CHARACTERISTICS OF THERMOCAPILLARY CONVECTION IN LIQUID BRIDGE WITH DYNAMIC INTERFACE UNDER ZERO GRAVITY

Zhipu WU[1], Tongtong BU[1], Jiantao SUN[1], Yong ZOU[1*], Xubing TANG[1], Xianshan HUANG[1], Shoujun DING[1*], Hulin HUANG[2]

[1] School of Microelectronics and Data Science, Anhui University of Technology, Ma'anshan, P. R China

[2] College of Astronautics, Nanjing University of Aeronautics and Astronautics, Nanjing, P. R China

[*] Corresponding authors; E-mail addresses: yong.zou@163.com (Y. Zou), sjding@ahut.edu.cn (S. Ding).

In this study, the volume of fluid (VOF) method was used to capture the free surface deformation of the liquid bridge. The temperature difference (ΔT) between the two ends of the liquid bridge and its height-diameter ratio (Hr) were varied, and the simulation results were combined with spectral analysis so as to investigate their effects on the shape of the interface of the liquid bridge. The results show that the interface shape of the liquid bridge is similar to a 'waist', which is wider at the top and bottom and slightly narrower in the middle. Additionally, two vortices with opposite and symmetric flow directions are formed in the liquid bridge. Notably, the dominant frequencies of the velocity and temperature oscillations in the liquid bridge are the same. With the increase of temperature difference and height-diameter ratio, the degree of deformation of the interface increases, but the rate of its increase gradually decreases. The velocity within the liquid bridge oscillates around a stable mean value (S), which increases with temperature difference and height-diameter ratio. Conversely, the dominant frequency of these velocity oscillations diminishes with elevated temperature difference and height-diameter ratio. Furthermore, at height-diameter ratio is 1.5, the main vortex within the liquid bridge splits from one vortex cell into two separate vortex cells.

Key words: *liquid bridge; thermocapillary convection; VOF; half-zone; free surface; numerical simulation*

1. Introduction

The floating zone (FZ) method represents a crucible-free crystal growth technique, which mitigates melt contamination from crucible materials and circumvents limitations associated with the melting point of the target single crystal. This approach is widely regarded as an essential and distinctive methodology for the industrial-scale synthesis of high-purity semiconductor-grade silicon (Si) single crystals [1-3]. In the investigation of melt convection during FZ crystal growth, two predominant models are utilized: the full-zone and half-zone liquid bridge models [4]. The full-zone model provides unique capabilities for detailed characterization of instability mechanisms in Marangoni flow under actual

floating-zone conditions, representing a significant advantage of this approach [5]. However, current investigations of thermocapillary convection in melt zones predominantly utilize the half-zone model, as it successfully captures the fundamental features of melt convection while offering substantially reduced computational complexity and faster simulation times [6,7]. Under normal gravity conditions, thermocapillary convection is often overshadowed by buoyancy-driven convection. In contrast, under microgravity conditions, thermocapillary convection becomes the dominant mode of fluid motion in the melt [8,9]. And the liquid bridge model, as a simplified model derived from the FZ technique, becomes a widely used model in the study of thermocapillary flow [10].

The full-zone model is extensively employed in numerical simulations of FZ techniques, including the conventional FZ method, optical floating zone (OFZ) method, and radio-frequency (RF) heated FZ method. These simulations primarily investigate melt convection dynamics, temperature field distribution, and electromagnetic field characteristics. Raming et al. [11] numerically investigated four different possibilities of applying static and alternating magnetic fields during industrial FZ growth of large Si crystals. Minakuchi et al. [12] investigated the effect of the FZ technique on solute Marangoni convection during the growth of Si_xGe_{1-x} crystals under zero gravity conditions by numerical simulations. Yan et al. [13] proposed a reduced-order finite element model for temperature field analysis in OFZ crystal growth. Through three-dimensional numerical analysis. Sabanskis et al. [14] investigated the coupled transport phenomena involving inert gas flow, melt convection, and dopant distribution in both gas and melt phases during FZ Si crystal growth. Zou et al. [15] systematically examined the influence of rotating magnetic fields on thermocapillary convection dynamics and dopant segregation behavior during zero gravity FZ growth of doped Si single crystals in a full-zone configuration. Through multiphysics modeling, Jin et al. [16] performed systematic numerical simulations to analyze the interaction between thermal solute Marangoni flows and radiative heat transfer in full-zone crystal growth systems under simulated zero gravity environments. Dossa et al. [17] formulated a verified OFZ growth model and obtained preliminary crystallization results using a prototype high-pressure single-lamp furnace system. The results demonstrate that the full-zone configuration better captures the thermal boundary conditions characteristic of practical FZ systems. However, this modeling approach presents a significant limitation: the inability to prescribe equatorial plane temperatures in advance. This limitation arises because the inherent convection and heat exchange mechanisms establish temperature gradients that subsequently drive surface flow dynamics.

In the half-zone model, the thermal gradient can be quantitatively controlled by prescribing fixed temperature boundary conditions at the upper and lower disks. Moreover, this model successfully captures the essential features of thermocapillary convection in the FZ. Shevtsova et al. [18] conducted combined experimental and numerical investigations of free surface dynamics in a 5 cSt silicone oil liquid bridge, quantifying the coupled effects of buoyancy-driven and thermocapillary convection on interface deformation. Huang et al. [19] conducted a comprehensive investigation of magnetic field effects (both transverse and cusp geometries) on surface-tension-driven flows and consequent free surface distortions in silicon liquid bridges. Jayakrishnan and Tiwari [20] conducted a comprehensive investigation of how ambient air currents and concomitant interfacial thermal transport modify surface-tension-driven convection patterns in high *Pr* fluid configurations. Through integrated numerical simulations and experiments, Yano and Nishino [21] assessed the relative influence of interfacial convective versus radiative heat transfer on Marangoni flow structures in high *Pr* (*Pr* = 67) liquid bridges in weightlessness. Through global linear stability analysis, Mendis et al. [22] determined the

instability thresholds for coupled thermal solute Marangoni convection in zero gravity environments using a Si_xGe_{1-x} half-zone liquid bridge model. Through theoretical analysis, Carrión et al. [23] investigated the stability characteristics of thermal convection in high *Pr* liquid bridge systems. The analysis included determination of the axisymmetric base flow solution and subsequent calculation of non-axisymmetric disturbance modes, with full consideration of base flow coupling and perturbation-induced interface deformations. Le et al. [24] investigated the onset and dynamic characteristics of oscillatory thermocapillary convection, systematically determining the critical conditions across varying volume ratios under both terrestrial and microgravity environments. Jin et al. [25] conducted systematic numerical studies of radiation-coupled thermal solute convection in a SiGe binary system using a half-zone model under simulated microgravity. Zou et al. [26] used numerical simulations to study solute-thermocapillary coupled convection in a half-zone liquid bridge model. Wang et al. [27] systematically investigated the effects of *Pr* variation and thermal boundary conditions on flow characteristics while maintaining a constant radius ratio of 0.5 throughout their study.

Although numerical simulation methods for thermocapillary convection in liquid bridges under microgravity or zero gravity conditions have been extensively studied, research on dynamic interfaces remains relatively limited. Furthermore, the deformation of free surfaces during FZ crystal growth under an argon (Ar) atmosphere has not yet been investigated numerically. This investigation employs the finite volume method for computational modeling, incorporating a VOF approach to accurately capture free surface evolution in the FZ system under zero gravity conditions. Using Si as the model material, we systematically evaluate the influence of imposed thermal gradients and geometric parameters (characterized by height-diameter ratios) on interfacial morphology dynamics in the FZ.

2. Physical and mathematical models

The physical model consists of an axisymmetric half-zone liquid bridge with a free interface, characterized by two coaxial discs of diameter φ positioned at the top and bottom, separated by a distance h as shown in Figure 1. The top and bottom discs are maintained at temperatures T_c and T_h, respectively, with a temperature difference of $\Delta T = T_h - T_c > 0$. A molten Si liquid bridge is formed between the two discs, and the height-diameter ratio of the liquid bridge is defined as $Hr = h/\varphi$. The liquid bridge is enveloped by Ar gas, and the liquid-gas interface is deformable. The dimensions of the liquid bridge model are 10 mm in height and 10 mm in length.

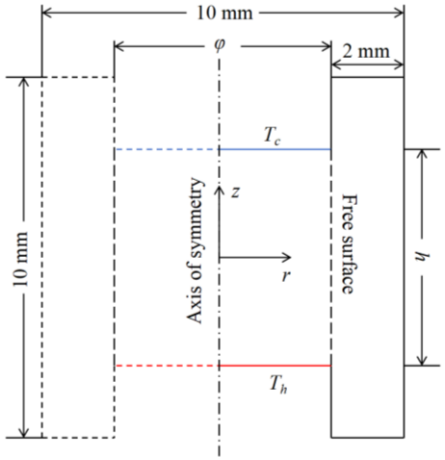

Figure 1 Physical model

To simplify the calculations, a few assumptions are made about the physical model: (1) the outer cylindrical region is set to be Ar, in which the flows of molten state Si and Ar are considered to be laminar; (2) the molten silicon in the middle is an incompressible Newtonian viscous fluid, and set the free interface between the two-phase flow; (3) the liquid bridge is under zero gravity; (4) the interface of the melt-Ar is deformable.

The surface tension at the interface is assumed to be a linear function of temperature:

$$\sigma = \sigma_0 - \sigma_T(T - T_0) \tag{1}$$

where σ_0 is the surface tension at $T = T_0$, σ_T is the temperature coefficient of surface tension, $\sigma_T = -\frac{\partial \sigma}{\partial T} > 0$. This assumption is widely applicable under conditions of small temperature differences [8][10][20][21][23].

Based on the above physical model and assumptions, the governing equations are given as follows [19]:

Continuity equation:

$$\frac{1}{r}\frac{\partial (ru)}{\partial r} + \frac{\partial w}{\partial z} = 0 \tag{2}$$

Momentum equations:

$$\frac{\partial u}{\partial t} + u\frac{\partial u}{\partial r} + w\frac{\partial u}{\partial z} = -\frac{1}{\rho}\frac{\partial p}{\partial r} + \mu\left[\frac{1}{r}\frac{\partial}{\partial r}\left(r\frac{\partial u}{\partial r}\right) + \frac{\partial^2 u}{\partial z^2} - \frac{u}{r^2}\right] \tag{3}$$

$$\frac{\partial w}{\partial t} + u\frac{\partial w}{\partial r} + w\frac{\partial w}{\partial z} = -\frac{1}{\rho}\frac{\partial p}{\partial z} + \mu\left[\frac{1}{r}\frac{\partial}{\partial r}\left(r\frac{\partial w}{\partial r}\right) + \frac{\partial^2 w}{\partial z^2}\right] \tag{4}$$

Energy equation:

$$\frac{\partial T}{\partial t} + u\frac{\partial T}{\partial r} + w\frac{\partial T}{\partial z} = \frac{\lambda}{\rho c_p}\left[\frac{1}{r}\frac{\partial}{\partial r}\left(r\frac{\partial T}{\partial r}\right) + \frac{\partial^2 T}{\partial z^2}\right] \tag{5}$$

where, u and w are velocity components in the r and z directions, respectively. t, ρ, p, T and c_p are the time, density, pressure, temperature and specific heat capacity, respectively; λ is the thermal conductivity; μ is the dynamic viscosity.

In the VOF method, phase distribution is represented by a scalar volume fraction field α (Eq. 6),

$$\begin{cases} \alpha = 0 & phase\ Ar \\ 0 < \alpha < 1 & interface \\ \alpha = 1 & phase\ Si \end{cases} \tag{6}$$

where α = 1 corresponds to complete fluid occupancy within a computational cell, α = 0 denotes pure gas phase, and intermediate values (0 < α < 1) identify interfacial regions [28]. The VOF method enables the accurate capture of complex interface topology changes and guarantees strict mass conservation for each fluid phase via the direct solution of the volume fraction transport equation.

3. Calculation conditions and methods

The simulation parameters, including boundary conditions and initialization settings, are outlined as follows: At the upper and lower interfaces of molten silicon, i.e. $T = T_c = 1685$ K for $z = h/2$ and $T = T_h$ for $z = -h/2$. The Ar interfaces are set as adiabatic walls, except for the upper and lower and free interfaces of molten silicon. At $t = 0$, $u = w = 0$, $T = T_c = 1685$ K. The region of molten Si is a column of diameter φ, defining the volume fraction of Si in the region $\alpha = 1$. The physical properties of both Si melt and Ar gas phases are tabulated in Table 1.

Table 1 Physical properties of the Si melt and Ar gas [6,7]

Parameters	Si	Ar
Density, ρ (Kg·m^{-3})	2530	1.63
Thermal conductivity, λ (W·m^{-1}·K^{-1})	67	0.018
Specific heat, c_p (J·Kg^{-1}·K^{-1})	1000	522
Dynamic viscosity, μ (Kg·m^{-1}·s^{-1})	7×10^{-4}	6.97×10^{-5}
Initial surface tension, σ_0 (N·m^{-1})	0.4868	-
Temperature coefficient of surface tension, σ_T (N·m^{-1}·K^{-1})	2.8×10^{-4}	-

The governing equations are numerically discretized using a finite volume formulation. To assess grid independence, simulations were conducted using six distinct grid configurations under the conditions of ΔT = 4 K and Hr = 1. The resulting maximum values of temperature and vorticity within the melt are presented in Figure 2(a). According to the verification of grid independence, and considering the accuracy and efficiency of calculation, a 1×10^5 grid is finally selected for numerical calculation. The maximum temperature and vorticity computed with the selected grid agree with the 2×10^5 grid solution to within 0.011% and 0.92%, respectively. Similarly, based on grid independence verification, grids of 9×10^4, 1.1×10^5, and 1.2×10^5 were employed for Hr = 0.75, 1.25, and 1.5, respectively. The discrete equations are solved iteratively using the velocity-pressure coupling method. To facilitate the coupling of velocity and pressure, the PISO algorithm is used, and the convective terms in the pressure equations are discretized using the PRESTO! format. The convective terms in both momentum and energy equations are discretized using the QUICK format, whereas gradient terms are approximated via a cell-centered Green-Gauss reconstruction method. The time step for iterations is set to 2×10^{-4} s and all simulations are completed by Ansys Fluent 2022. A comparative analysis, presented in Figure 2(b), is conducted to validate the numerical methodology employed in this investigation. The free-surface shape of the liquid bridge obtained in this study is in better agreement with the results reported by Sim et al. [8]. Furthermore, as shown in Figure 3, the high consistency between the numerical and experimental results verifies the fidelity of the simulated free interface shape and the gas phase flow field [29,30].

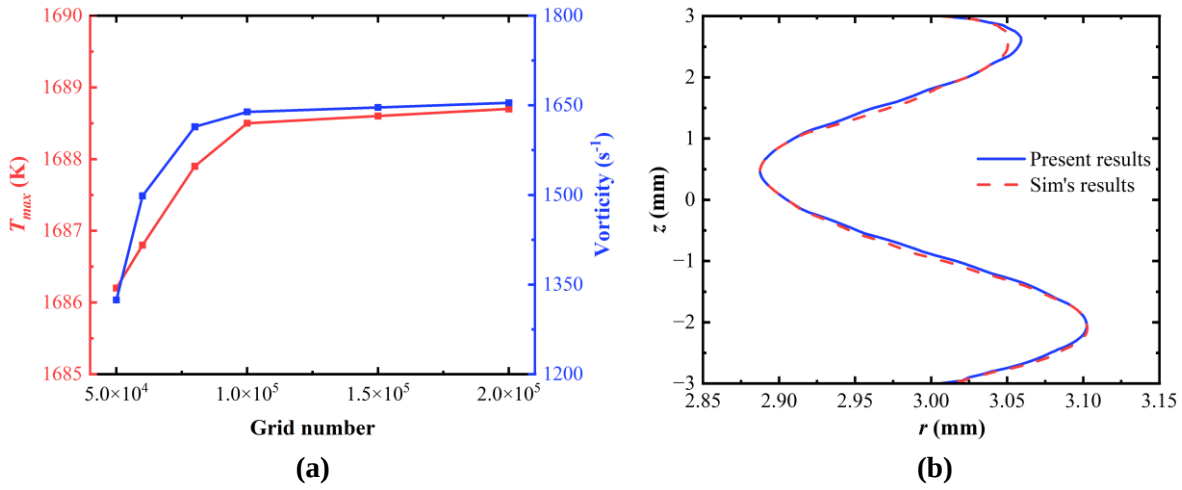

Figure 2 (a) Mesh independence verification curve, (b) comparison of free surface of liquid bridge

(a) **(b)** **(c)**

Figure 3 (a) Free interface shape and gas-liquid streamline in this study, (b) free interface shape and gas streamline in reference [29], (c) free interface shape in reference [30]

4. Calculation results

4.1. Melt velocity field versus temperature field and free interface deformation characteristics

The temperature distribution of the liquid bridge with Hr = 1 and ΔT = 4 K is illustrated in Figure 4(a). It can be seen that the temperature distribution is in the shape of 'M' in the whole, and in the shape of 'V' in the liquid bridge. This indicates that heat transfer occurs more rapidly at the surface compared to the center, a phenomenon closely associated with the fluid flow dynamics. Figure 4(b) depicts the convection patterns within the liquid bridge in the context of temperature, where two vortices with opposite and symmetrical flow directions are formed in the Si melt and Ar zones, respectively. Specifically, the vortex on the left side of the Si melt flows clockwise, corresponding to the vortex on the right side of the Ar zone, while the vortex on the right side of the Si melt flows counterclockwise, corresponding to the vortex on the left side of the Ar zone. Under zero gravity conditions, natural convection driven by gravity is negligible. In the half-zone liquid bridge configuration, the imposed temperature gradient generates a surface tension gradient along the liquid-gas interface due to the linear temperature dependence of surface tension. This gradient, characterized by diminished surface tension at the heated end compared to the cooled end, produces a stress that drives interfacial transport toward the cooler region and initiates bulk thermocapillary convection [31].

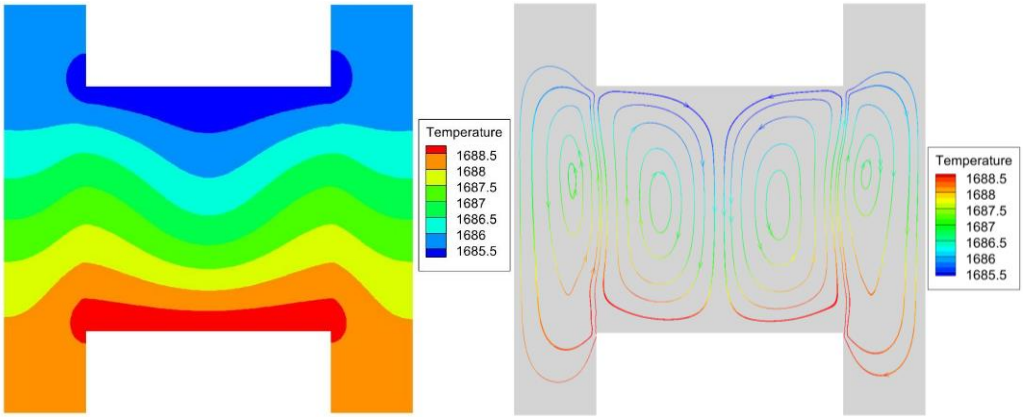

Figure 4 (a) Temperature distribution cloud of the liquid bridge; (b) the velocity streamline of the liquid bridge in the context of temperature

A monitoring point at coordinates (2 mm, 0) was selected for velocity and temperature measurements to gain deeper insights into the temporal evolution of internal fluid flow. Figure 5(a) demonstrates that during the initial development phase (t < 0.85 s), both the velocity magnitude and temperature at the monitoring location show a consistent monotonic increase. Beyond 0.85 s, the velocity and temperature begin to oscillate, with the oscillation amplitude varying over time. The velocity and temperature time-series data recorded at the monitoring point (2 mm, 0) during the 7-9 s interval were subjected to Fast Fourier Transform (FFT) analysis, and the resulting spectral is presented in Figure 5(b). The dominant frequency of the fluid velocity oscillation is identified as 8.01 Hz. Similarly, the dominant frequency of the temperature oscillation is also found to be 8.01 Hz, matching that of the velocity oscillation. This agreement underscores the interconnection between thermocapillary convection and temperature distribution [10].

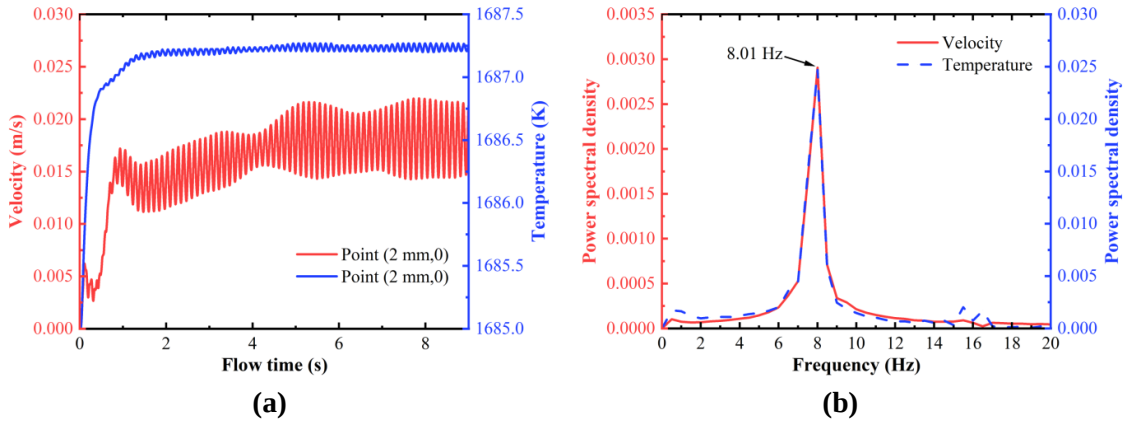

Figure 5 (a) Time evolutions of velocity and temperature at monitoring point; (b) the spectral of velocity and temperature at the monitoring point over a 7-9 second time period

Figure 6 depicts the periodic evolution of the liquid bridge interface morphology over one complete oscillation cycle. The interface exhibits a distinct ‘waist’ shape, characterized by a larger radius at the ends compared to the middle section. For example, at 8.20 s, the ‘waist’ shape is less

pronounced. Between 8.22 s and 8.26 s, the lower end of the 'waist' becomes slightly wider than the upper end, whereas at 8.28 s, the widths of the upper and lower sections of the 'waist' are nearly equal. Overall, the interface shape of the liquid bridge was consistently similar to the 'waist' shape.

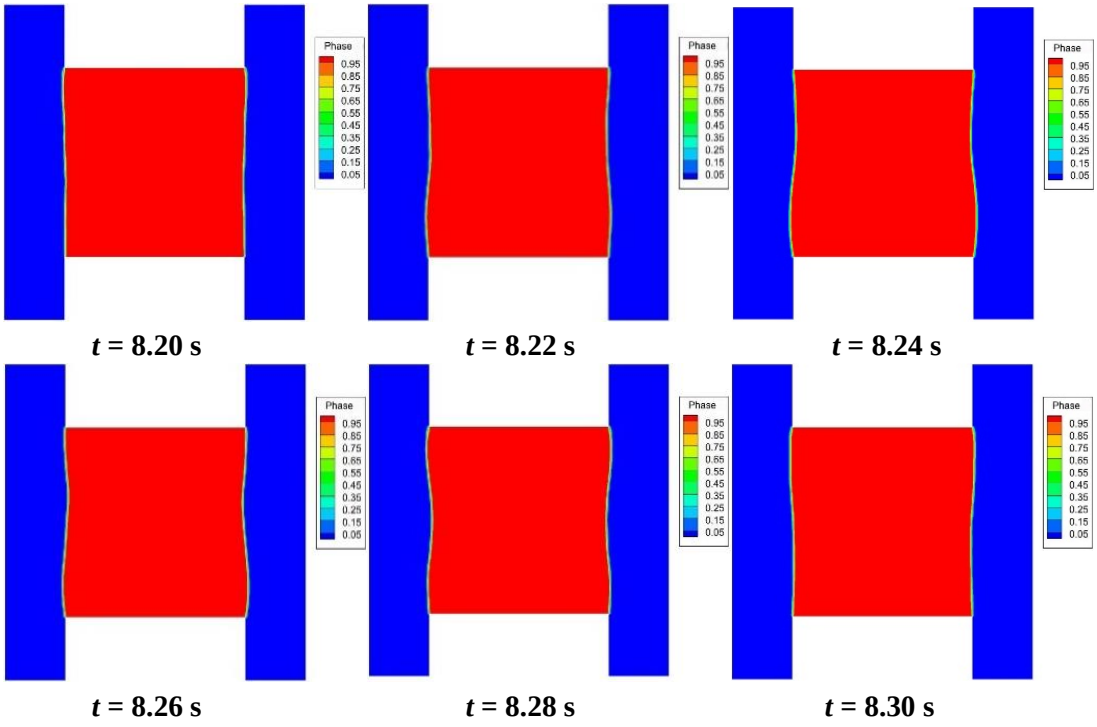

Figure 6 The interface deformation diagram of the liquid bridge within one cycle

4.2. Dynamic characteristics of thermocapillary convection at different temperature differences and its effect on interfacial deformation

Under zero gravity conditions, thermocapillary convection dominates as the primary mode of fluid motion within the liquid bridge and is highly sensitive to variations in ΔT between the two ends. Next, this study will examine how ΔT affects the velocity and temperature distributions in a dynamic interfacial liquid bridge with an *Hr* of 1. Specifically, the analysis explores ΔT's role in governing the stability of thermocapillary convection and the kinematic behavior of free interface deformation.

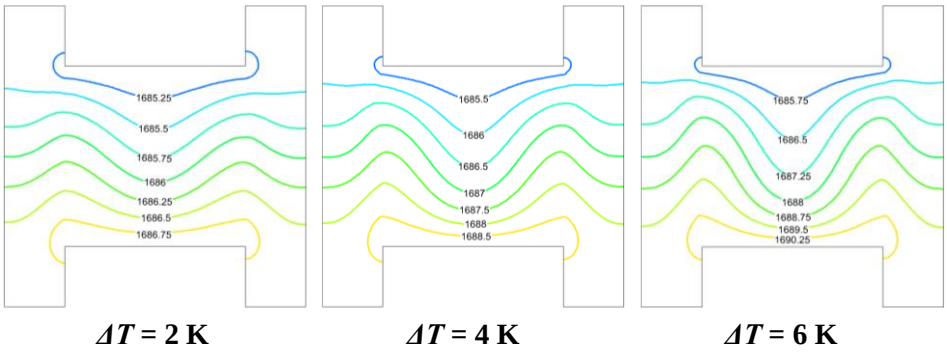

Figure 7 Isotherm plots at different temperature differences

The isotherm distributions within the liquid bridge at varying temperature differences are depicted in Figure 7. Thermocapillary convection within the liquid bridge generates two counter-rotating vortices, causing surface fluid to flow from the high-temperature region to the low-temperature region, while the central fluid flows in the opposite direction. This flow pattern results in significant distortion of the isotherms, characterized by a sharp, narrow low-temperature band at the center and high-temperature bands on both sides, collectively forming a 'V'-shaped profile. As evident from Figure 7, increasing the temperature difference amplifies the distortion of the isotherms, causing the lower portion of the 'V' shape to become more sharper and narrower.

Figure 8 presents the velocity oscillations observed at the monitoring point (2 mm, 0) for ΔT of 2 K, 4 K, and 6 K at Hr = 1, analyzed over the time interval of 5-10 s. The results demonstrate three key characteristics of the oscillatory behavior. Firstly, in all three cases, the velocity oscillates around a stable mean value (S) that scales with the applied temperature difference--higher ΔT values yield larger mean velocities. Secondly, the oscillation amplitude shows distinct ΔT dependence. At ΔT = 2 K, the amplitude exhibits marked temporal variability, while at ΔT = 6 K, the amplitude stabilize significantly, approaching a quasi-steady state. Thirdly, spectral analysis (Figure 9) reveals a systematic decrease in the dominant oscillation frequency with increasing ΔT: from 8.4 Hz (ΔT = 2 K) to 7.8 Hz (ΔT = 4 K), and further to 7.0 Hz (ΔT = 6 K).

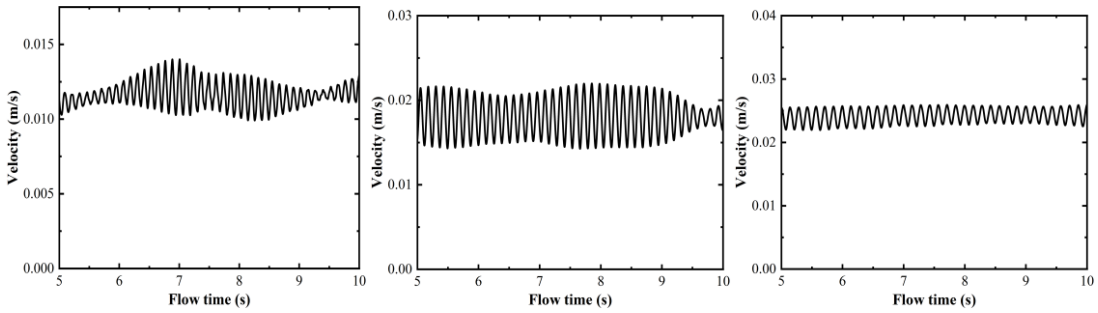

Figure 8 Velocity versus time curves for the monitoring point (2 mm, 0) under different temperature differences

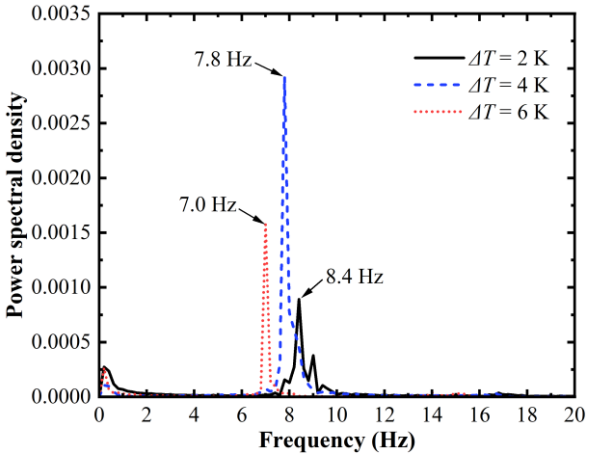

Figure 9 Spectral analysis plot under ΔT = 2 K, 4 K, 6 K

Figure 10 illustrates the deformation profiles of the liquid bridge at its maximum deformation state for ΔT of 2 K, 4 K, and 6 K at Hr = 1. The liquid bridge exhibits outward bulging near its ends, while the central region remains inwardly concave, forming a distinct 'waist' shape, consistent with the results shown in Figure 6. As the ΔT increases, the extent of both the outward bulging and inward depression at the interface becomes more pronounced, which is consistent with previous studies [18]. In order to better describe the change of interface deformation with temperature difference, the interface deformation rate ε is defined as:

$$\varepsilon = \frac{\varphi_{max} - \varphi_{min}}{\varphi} \tag{7}$$

where: φ_{max} is the maximum diameter of liquid bridge deformation, φ_{min} is the minimum diameter of liquid bridge deformation.

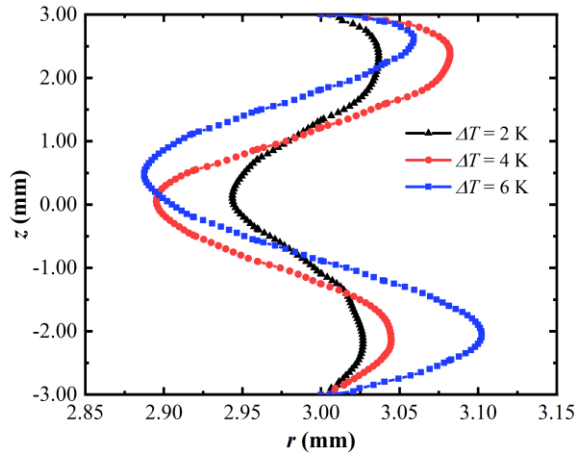

Figure 10 The unilateral interface deformation under different ΔT conditions

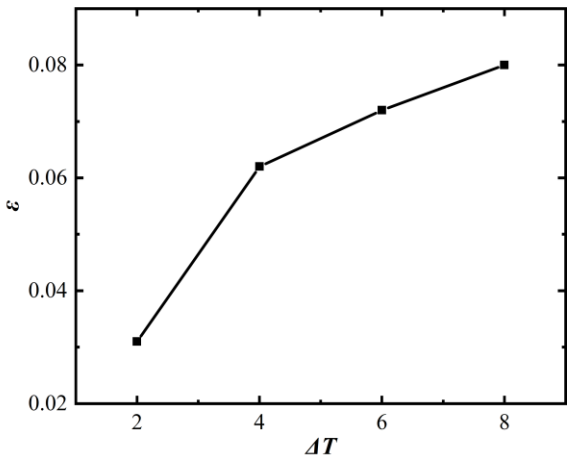

Figure 11 Curve of interfacial deformation rate with ΔT

The deformation rate of the liquid-bridge interface at varying temperature differences is shown in Figure 11. It is evident that the deformation rate ε increases with the ΔT, indicating a greater degree of interfacial deformation. Specifically, the deformation rate doubles as ΔT increases from 2 K to 4 K, rises by a factor of 1.15 as ΔT increases from 4 K to 6 K, and further increases by a factor of 1.11 as ΔT

increases from 6 K to 8 K. These results demonstrate that the rate of increase in the deformation rate gradually diminishes as the ΔT rises from 2 K to 8 K.

4.3 Dynamic characteristics of thermocapillary convection at different aspect ratios and its effect on interfacial deformation

Under zero gravity conditions, thermocapillary forces become the predominant driver of fluid motion in liquid bridge systems, and the structure of the flow field is significantly influenced by *Hr* [7]. Figure 12 depicts the velocity oscillations at the monitoring point (2 mm, 0) over the time interval of 5-15 s for varying *Hr* at ΔT = 4 K. In all three cases, the velocity oscillates around a stable mean value (S) that increases monotonically with *Hr*, demonstrating a *Hr* dependence. The spectral analysis of these velocity oscillations is presented in Figure 13. For *Hr* = 0.75, the dominant frequency of the velocity oscillation is 12.5 Hz, with an average amplitude of 0.736 mm/s; for *Hr* = 1, the dominant frequency decreases to 7.8 Hz, with an average amplitude of 2.90 mm/s; and for *Hr* = 1.25, the dominant frequency further decreases to 7.6 Hz, with an average amplitude of 5.65 mm/s. The results reveal an inverse relationship between *Hr* and oscillation frequency, accompanied by a positive correlation with oscillation amplitude. It suggests that increasing *Hr* suppresses the dominant frequency of velocity oscillations in thermocapillary convection while enhancing its average amplitude.

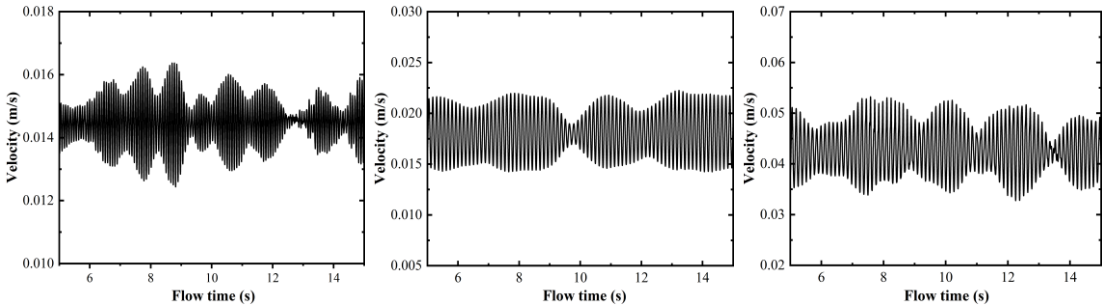

Figure 12 Velocity versus time curves for the monitoring point (2 mm, 0) under different height-diameter ratios

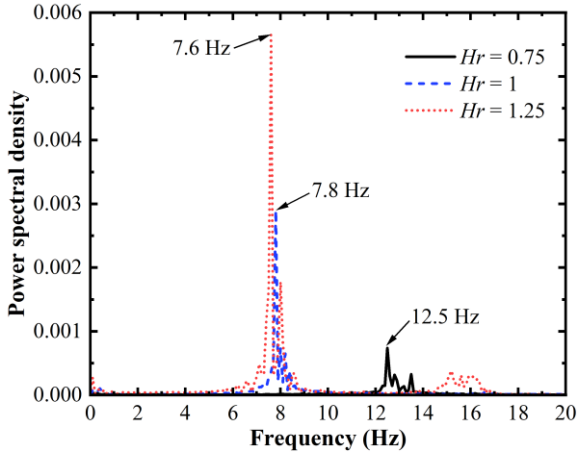

Figure 13 Spectral analysis plot under the conditions of *Hr* = 0.75, 1, 1.25

The velocity streamlines within the liquid bridge at varying height-diameter ratios in the context of volume fraction are illustrated in Figure 14. For *Hr* = 0.75, 1 and 1.25, two symmetric but opposite flow direction vortex cells were formed in the liquid bridge, which is consistent with the vortex distribution observed in Figure 4(b) under the temperature background. Furthermore, the interfacial deformation becomes increasingly significant as the *Hr* increases, exhibiting a clear *Hr*-dependent enhancement. As *Hr* increases, the main vortices in the liquid bridge stretch along the axial direction [32]. At *Hr* = 1.5, the two main vortices within the liquid bridge undergo a distinct bifurcation, splitting from a single vortex cell into two separate vortex cells. This phenomenon, characterized by the emergence of dual vortices, was previously reported by Yano et al. [33] and is regarded as a distinctive feature of liquid bridges with high *Hr* values. Figure 15 presents the deformation rate of the liquid bridge interface at different height-diameter ratios, revealing that the deformation rate increases with *Hr*. Specifically, the deformation rate increases by a factor of 2.22 as *Hr* rises from 0.75 to 1, by a factor of 1.47 as *Hr* increases from 1 to 1.25, and by a factor of 1.11 as *Hr* further increases from 1.25 to 1.5. These results demonstrate that the rate of increase in the deformation rate gradually diminishes as *Hr* increases from 0.75 to 1.5.

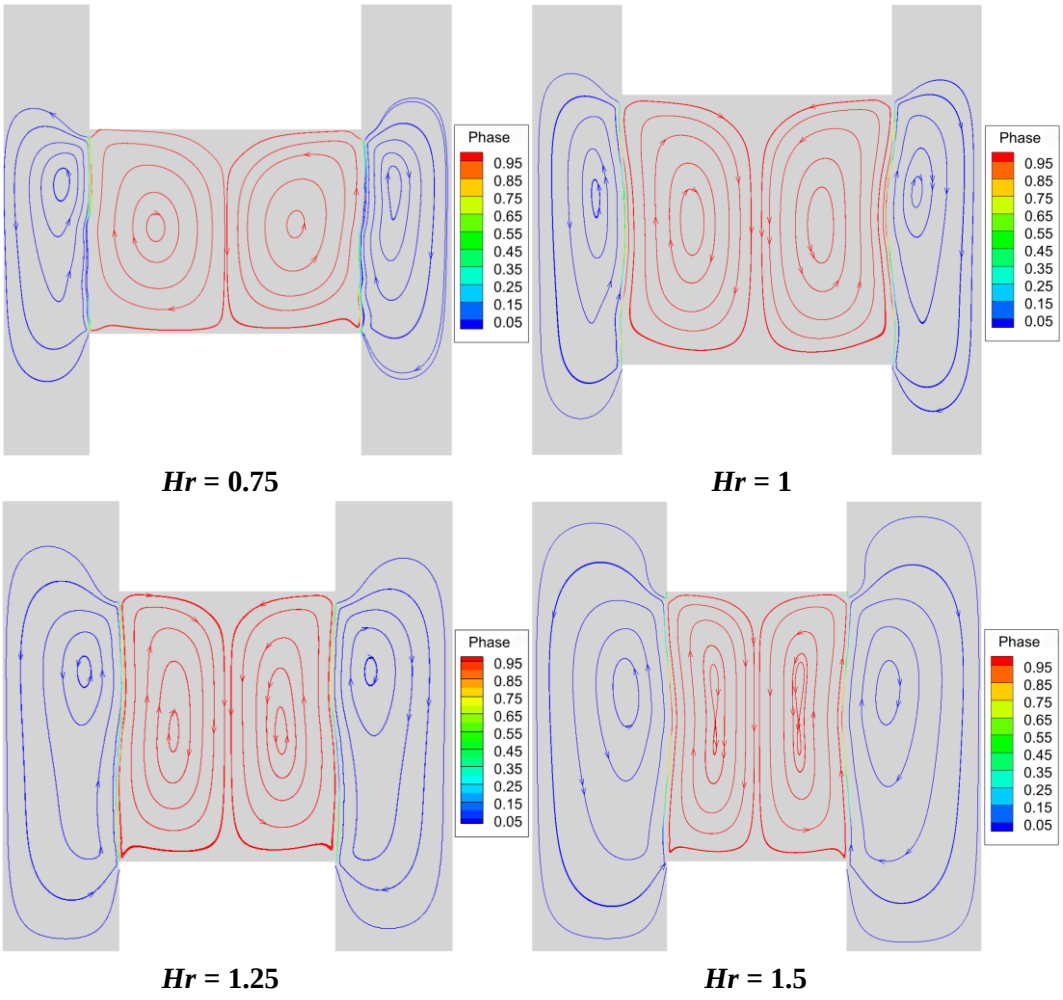

Figure 14 The velocity streamline at different height-diameter ratios in the context of volume fraction

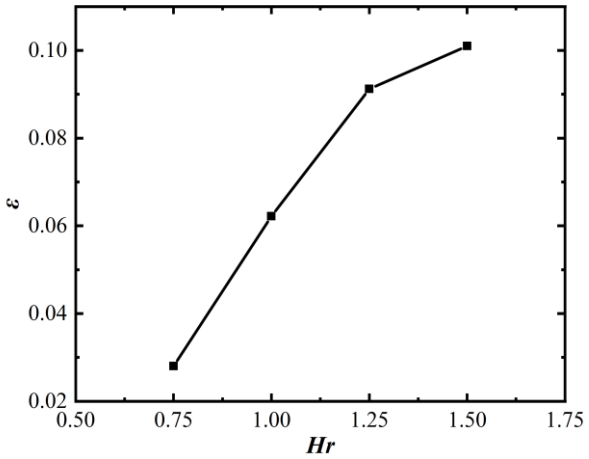

Figure 15 Curve of interfacial deformation rate as a function of *Hr*

5. Conclusion

This study employs computational modeling to investigate free-surface deformation dynamics in liquid bridge systems under zero gravity conditions. The effects of varying temperature differences (ΔT = 2 K, 4 K, 6 K, and 8 K) and height-diameter ratios (Hr = 0.75, 1, 1.25, and 1.5) on the free-surface deformation are examined. As a primarily theoretical investigation that assumes a linear surface tension-temperature relationship, the analysis is consequently confined to scenarios with small temperature differences. Thus, the findings may not be directly applicable to industrial crystal growth conditions. The key findings of this work are summarized below:

(1) The temperature distribution for Hr =1 and ΔT = 4 K exhibit an overall 'M'-shaped profile, with a 'V'-shaped pattern observed within the liquid bridge. The interface of the liquid bridge adopts a distinct 'waist' shape. Concurrently, two counter-rotating vortices with symmetrical flow directions form within the liquid bridge, a phenomenon attributed to the dominance of thermocapillary convection under zero gravity conditions. Spectral analysis of the monitoring points reveals that the dominant frequency of both velocity and temperature oscillations is 8.01 Hz, further confirming the interconnection between thermocapillary convection and temperature distribution.

(2) As the ΔT increases, the distortion of the isotherms within the liquid bridge becomes more pronounced, resulting in a sharper and narrower lower section of the 'V'-shaped profile. The velocity oscillations within the liquid bridge fluctuate around a stable mean value (S), which increases with ΔT. In addition, spectral analysis reveals that the dominant frequency of the velocity oscillations decreases from 8.4 Hz to 7.0 Hz as ΔT increases. Concurrently, the interfacial deformation of the liquid bridge becomes more pronounced with higher ΔT, though its rate of deformation exhibits a gradual decline.

(3) When the Hr increases from 0.75 to 1.25, the average amplitude of the velocity oscillations at the monitoring point rises from 0.736 mm/s to 5.65 mm/s, but the dominant frequency of the oscillation decreases from 12.5 Hz to 7.6 Hz. Furthermore, at Hr = 1.5, the two main vortices within the liquid bridge undergo a distinct bifurcation, splitting from a single vortex cell into two separate vortex cells. This phenomenon is regarded as a unique characteristic of liquid bridges with high Hr values. Similarly, the interfacial deformation of the liquid bridge intensifies with increasing Hr, albeit at a diminishing rate.

Acknowledgements

This work is supported by the National Natural Science Foundation of China (52202001), University Outstanding Youth Research Project of Anhui Province (2024AH030007), Major Special Project of Science and Technology of Anhui Province (202203a05020002) and University Natural Science Research Project of Anhui Province (KJ2021A0388). Natural Science Research Project of Anhui Province Education Department for Excellent Young Scholars (S.J. Ding, 2024) supported this study.

References

[1] Lan, C.W., Chian, J.H., Three-Dimensional Simulation of Marangoni Flow and Interfaces in Floating-Zone Silicon Crystal Growth, *Journal of Crystal Growth*, *230* (2001), 1-2, pp. 172-180

[2] Surovovs, M., *et al*., Numerical Modelling of Melting Front Structures during Floating Zone Silicon Crystal Growth, *Journal of Crystal Growth*, *643* (2024), pp. 127788

[3] Kranert, C., *et al*., Facet Growth Kinetics and Diameter Fluctuations in Molten Zone Si Crystal Growth, *Journal of Crystal Growth*, *652* (2025), pp. 128024

[4] Jayakrishnan, R., Tiwari, S., On Three-Dimensional Flow Structures and Oscillatory Instability due to Free Surface Heat Loss in Half-Floating Zones under Microgravity, *Advances in Space Research*, *67* (2021), 10, pp. 3354-3377

[5] Agampodi Mendis, R.L., *et al*., The Relative Contribution of Solutal Marangoni Convection to Thermal Marangoni Flow Instabilities in a Liquid Bridge of Smaller Aspect Ratios under Zero Gravity, *Crystals*, *11* (2021), 2, pp. 116

[6] Zhang, Y., *et al*., Effect of Marangoni Number on Thermocapillary Convection and Free-Surface Deformation in Liquid Bridges, *Journal of Thermal Science*, *25* (2016), 2, pp. 178-187

[7] Fan, J.G., Liang, R.Q., Numerical Simulation of Thermocapillary Convection in a Half-Zone Liquid Bridge Model with Large Aspect Ratio under Microgravity, *Symmetry*, *14* (2022), 3, pp. 452

[8] Sim, B.C., *et al*., Dynamic Free-Surface Deformations in Axisymmetric Liquid Bridges, *Advances in Space Research*, *34* (2004), 7, pp. 1627-1634

[9] Kang, Q., *et al*., Space Experimental Study on Wave Modes under Instability of Thermocapillary Convection in Liquid Bridges on Tiangong-2, *Physics of Fluids*, *32* (2020), 3, pp. 34107

[10] Chen, S., *et al*., Dynamic Mode Decomposition of Thermocapillary Convection in GaAs Melt Liquid Bridge between Unequal Ends, *International Journal of Heat and Mass Transfer*, *216* (2023), pp. 124612

[11] Raming, G., *et al*., Numerical Investigation of the Influence of EM-Fields on Fluid Motion and Resistivity Distribution during Floating-Zone Growth of Large Silicon Single Crystals, *Journal of Crystal Growth*, *230* (2001), 1, pp. 108-117

[12] Minakuchi, H., *et al*., A Three-Dimensional Numerical Simulation Study of the Marangoni Convection Occurring in the Crystal Growth of Si_xGe_{1-x} by the Float-Zone Technique in Zero Gravity, *Journal of Crystal Growth*, *266* (2004), 1-3, pp. 140-144

[13]Yan, Y.Z., *et al*., A Simplified Finite Element Model for Numerical Simulation of Temperature Field and Optimization of Parameters in Single Crystal Growth by Optical Floating Zone Technique, *Journal of Crystal Growth*, *468* (2017), pp. 923-932

[14]Sabanskis, A., *et al*., 3D Modeling of Doping from the Atmosphere in Floating Zone Silicon Crystal Growth, *Journal of Crystal Growth*, *457* (2017), pp. 65-71

[15]Zou, Y., *et al*., Effect of Rotating Magnetic Field on Thermal Convection and Dopant Transport in Floating-Zone Crystal Growth, *Microgravity Science and Technology*, *32* (2020), 3, pp. 349-361

[16]Jin, C.H., *et al*., Numerical Simulation of Thermo-Solutal Marangoni Convection in a Full Floating Zone with Radiative Heat Transfer under Zero Gravity, *Journal of Crystal Growth*, *570* (2021), pp. 126204

[17]Dossa, S.S., Derby, J.J., Modeling Optical Floating Zone Crystal Growth in a High-Pressure, Single-Lamp Furnace, *Journal of Crystal Growth*, *591* (2022), pp. 126723

[18]Shevtsova, V., *et al*., Subcritical and Oscillatory Dynamic Surface Deformations in Non-Cylindrical Liquid Bridges, *Fluid Dynamics & Materials Processing*, *4* (2008), 1, pp. 43-54

[19]Huang, H.L., *et al*., Thermocapillary Flow and Free-Surface Deformation of Liquid Bridge under Different Magnetic Fields, *Applied Thermal Engineering*, *135* (2018), pp. 83-94

[20]Jayakrishnan, R., Tiwari, S., Influence of Co-Axial Airflow and Volume Ratio on Thermo-Capillary Convection in Half Floating Zones, *Computers & Fluids*, *179* (2019), pp. 248-264

[21]Yano, T., Nishino, K., Numerical Study on the Effects of Convective and Radiative Heat Transfer on Thermocapillary Convection in a High-Prandtl-Number Liquid Bridge in Weightlessness, *Advances in Space Research*, *66* (2020), 8, pp. 2047-2061

[22]Mendis, R.L.A., *et al*., Global Linear Stability Analysis of Thermo-Solutal Marangoni Convection in a Liquid Bridge under Zero Gravity, *Microgravity Science and Technology*, *32* (2020), 4, pp. 729-735

[23]Carrión, L.M., *et al*., Influence of the Dynamical Free Surface Deformation on the Stability of Thermal Convection in High-Prandtl-Number Liquid Bridges, *International Journal of Heat and Mass Transfer*, *146* (2020), pp. 118831

[24]Le, C.C., *et al*., Oscillatory Thermocapillary Convection in Deformed Half Zone Liquid Bridges of Low Prandtl Number Fluids, *International Communications in Heat and Mass Transfer*, *127* (2021), pp. 105499

[25]Jin, C., *et al*., Numerical Simulation of Thermo-Solutal Marangoni Convection in a Floating Half-Zone with Radiation Effects under Zero Gravity, *International Journal of Heat and Mass Transfer*, *194* (2022), pp. 123010

[26]Zou, Y., *et al*., Effect of Aspect Ratio on Coupled Solute-Thermocapillary Convection Instability in Half-Zone Liquid Bridge, *Thermal Science*, *26* (2022), 6, pp. 4489-4502

[27]Wang, Y., *et al*., Effect of Prandtl Number on the Flow Instabilities in Thermocapillary Liquid Bridges between two Coaxial Disks with Different Radii, *International Journal of Heat and Mass Transfer*, *205* (2023), pp. 123895

[28]Yan, S.L., *et al.*, Adaptive Mesh Refinement for VOF Modeling Gas-Liquid Two-Phase Flow: A Summary of Some Algorithms and Applications, *Chemical Engineering Science*, *306* (2025), pp. 121291

[29]Selver, R., Experiments on the Transition from the Steady to the Oscillatory Marangoni Convection of a Floating-Zone under Various Cold Wall Temperatures and Various Ambient Air Temperature Effects, *Microgravity Science and Technology*, *17* (2005), 4, pp. 25-35

[30]Cheng, M., Kou, S., Detecting Temperature Oscillation in a Silicon Liquid Bridge, *Journal of Crystal Growth*, *218* (2000), 1, pp. 132-135

[31]Minakuchi, H., *et al*., Three-Dimensional Numerical Simulation of Thermal and Solutal Marangoni Convection in a Liquid Bridge under Zero-Gravity Field, *Aerospace Technology Japan*, *10* (2012), 28, pp. 15-20

[32]Zhang, Y., *et al*., The Effect of Aspect Ratio and Axial Magnetic Field on Thermocapillary Convection in Liquid Bridges with a Deformable Free-Surface, *Engineering Applications of Computational Fluid Mechanics*, 10 (2015), 1, pp. 16-28

[33]Yano, T., *et al*., 3-D PTV Measurement of Marangoni Convection in Liquid Bridge in Space Experiment, *Experiments in Fluids*, *53* (2011), 1, pp. 9-20

Submitted: 12.9.2025.

Revised: 09.10.2025.

Accepted 16.10.2025.